Supplement of

Global distribution of tetrafluoromethane (CF_4) and hexafluoroethane (C_2F_6) emissions determined by inverse modeling

Benjamin Püschel et al.

S1 Measurement data

ID	Station name	Organisation/ Source	Location	Altitude [m.a.s.l.]	Sampling frequency	Period
CGO	Cape Grim, Tasmania	AGAGE	40.7°S, 144.7°E	94	2h	01.2006-12.2023
CMN	Monte Cimone, Italy	AGAGE	44.2°N, 10.7°E	2165	2h	10.2022-12.2023
GSN	Gosan, South Korea	AGAGE	33.3°N, 126.2°E	72	2h	11.2007-12.2019
JFJ	Jungfraujoch, Switzerland	AGAGE	46.5°N, 8.0°E	3559	2h	04.2008-12.2023
MHD	Mace Head, Ireland	AGAGE	53.3°N, 9.9°W	8	2h	01.2006-12.2023
RPB	Ragged Point, Barbados	AGAGE	13.2°N, 59.4°W	30	2h	01.2006-12.2023
SDZ	Shangdianzi, China	CMA	40.7°N, 117.1°E	291	2h	01.2011-12.2021
SMO	Cape Matatula, American Samoa	AGAGE	14.2°S, 170.6°W	42	2h	12.2006-12.2023
TAC	Tacolneston, United Kingdom	AGAGE	52.5°N, 1.1°E	64	2h	12.2012-12.2023
THD	Trinidad Head, USA	AGAGE	41.1°N, 124.2°W	107	2h	01.2006-12.2023
TOB	Taunus, Germany	AGAGE	50.2°N, 8.4°E	825	2h	02.2023-12.2023
ZEP	Zeppelin, Norway	AGAGE	78.9°N, 11.9°E	475	2h	09.2010-12.2023

Table S1. Sites of continuous atmospheric measurements of CF_4 and C_2F_6.

ID	Station name	Organisation/ Source	Location	Altitude [m.a.s.l.]	Sampling frequency	Period
AKD	Akedala, China	CMA	47.1°N, 87.6°E	562m	1w	08.2017-10.2021
ALT	Alert, Canada	NOAA-ESRL-GML	82.5°N, 62.5°W	185m	1w	10.2014-12.2023
AMY	Anmyeon-do, South Korea	NOAA-ESRL-GML	36.5°N, 126.3°E	47m	3m	12.2018-07.2021
BRW	Barrow, USA	NOAA-ESRL-GML	71.3°N, 156.6°W	11m	2w	10.2014-12.2023
HFM	Harvard Forest, USA	NOAA-ESRL-GML	42.5°N, 72.2°W	340m	2w	11.2014-12.2023
JGJ	Jiangjin, China	CMA	29.2°N, 106.2°E	262m	1d	03.2017-12.2021
JSA	Jinsha, China	CMA	29.6°N, 114.2°E	750m	1w	01.2019-11.2021
KUM	Cape Kumukahi, USA	NOAA-ESRL-GML	19.6°N, 154.9°W	8m	2m	09.2014-08.2021
LAN	Lin'an, China	CMA	30.3°N, 119.7°E	138m	1d	01.2011-11.2021
LEF	Park Falls, USA	NOAA-ESRL-GML	45.9°N, 90.3°W	472m	2w	10.2014-12.2023
LFS	Longfengshan, China	CMA	44.7°N, 127.6°E	330m	1w	01.2011-10.2021
MLO	Mauna Loa, USA	NOAA-ESRL-GML	19.5°N, 155.6°W	3397m	2w	09.2014-11.2022
NWR	Niwot Ridge, USA	NOAA-ESRL-GML	40.1°N, 105.6°W	3523m	1w	11.2014-12.2023
PSA	Palmer Station, Antarctica	NOAA-ESRL-GML	64.8°S, 64.1°W	10m	1m	07.2014-12.2023
SPO	South Pole, Antarctica	NOAA-ESRL-GML	90.0°S, 24.8°W	2810m	2w	02.2014-12.2023
SUM	Summit, Greenland	NOAA-ESRL-GML	82.6°N, 38.4°W	3210m	2w	08.2014-12.2023
TRL	Trollhaugen, Antarctica	NILU	72.0°S, 2.5°W	1558m	1m	03.2008-12.2023
XCG	Xichong, China	Chen (2025)	22.5°N, 114.6°E	137	1d	10.2021-12.2023

Table S2. Sites of atmospheric flask measurements of CF_4 and C_2F_6.

ID	Station name	Organisation/ Source	Location	Altitude [m.a.s.l.]	Sampling frequency	Period
AMT	Argyle, USA	NOAA-ESRL-GML	45.0°N, 68.7°W	52m	2d	01.2015-12.2023
BWD	Brentwood, USA	NOAA-ESRL-GML	38.9°N, 77.0°W	17m	2d	12.2018-12.2023
CRV	Fairbanks, USA	NOAA-ESRL-GML	65.0°N, 147.6°W	611m	2d	09.2015-12.2023
LEF	Park Falls, USA	NOAA-ESRL-GML	45.9°N, 90.3°W	472m	2d	01.2015-12.2023
LEW	Lewisburg, USA	NOAA-ESRL-GML	40.9°N, 76.9°W	166m	2d	10.2015-12.2023
MBO	Mt. Bachelor, USA	NOAA-ESRL-GML	44.0°N, 121.7°W	2731m	1d	09.2015-12.2023
MKO	Mauna Kea, USA	NOAA-ESRL-GML	19.8°N, 155.5°W	4199m	2d	12.2022-12.2023
MRC	Marcellus, USA	NOAA-ESRL-GML	41.5°N, 76.4°W	592m	2d	08.2015-12.2023
MSH	Mashpee, USA	NOAA-ESRL-GML	41.7°N, 70.5°W	32m	3d	05.2016-12.2023
MWO	Mt. Wilson, USA	NOAA-ESRL-GML	34.2°N, 118.1°W	1729m	1d	03.2015-12.2023
NEB	Baltimore, USA	NOAA-ESRL-GML	39.3°N, 76.6°W	44m	2d	04.2018-12.2023
NWB	Baltimore, USA	NOAA-ESRL-GML	39.3°N, 76.7°W	135m	2d	04.2018-12.2023
SCT	Beech Island, USA	NOAA-ESRL-GML	33.4°N, 81.8°W	115m	2d	01.2015-12.2023
SGP	Southern Great Plains, USA	NOAA-ESRL-GML	36.6°N, 97.5°W	314m	4d	11.2016-12.2023
STR	San Francisco, USA	NOAA-ESRL-GML	37.8°N, 122.5°W	254m	12h	03.2015-12.2023
TMD	Thurmont, USA	NOAA-ESRL-GML	39.6°N, 77.5°W	561m	4d	08.2017-12.2023
WBI	West Branch, USA	NOAA-ESRL-GML	41.7°N, 91.4°W	242m	2d	03.2015-12.2023
WGC	Walnut Grove, USA	NOAA-ESRL-GML	38.3°N, 121.5°W	2m	2d	01.2015-12.2023
WKT	Moody, USA	NOAA-ESRL-GML	31.3°N, 97.3°W	251m	2d	01.2015-12.2023

Table S3. Sites of additional atmospheric flask measurements of CF_4.

S2 Global reanalysis simulation

The FLEXPART11 Linear Chemistry Module (LCM) simulates atmospheric transport in a global domain, filled with particles that are constantly advected throughout the atmosphere in a forward-in-time mode. We release 50 million homogeneously distributed particles, each carrying masses of CF_4 and C_2F_6 from which the dry air mole fraction can be calculated. Particle masses are initialized using a latitudinal profile of atmospheric mole fractions, reducing necessary spin-up time compared to an initialization of a constant value. The latitudinal profiles are derived from linear interpolation between background measurements within a 30 d window around the simulation start date (Vojta et al., 2022). Ideally, a single simulation would be performed for the entire study period, but computational constraints necessitate annual subdivisions with each year simulated in parallel. This approach requires reinitialization and a repeated two-month spin-up period for each year.

To account for emissions occurring during the simulation period, LCM does not release new particles, but instead adds emitted tracer mass to passing particles near the emission source grid cell (Bakels et al., 2024; Groot Zwaaftink et al., 2018). Emission data given to FLEXPART11 LCM was based on the EDGARv8.0 (EDGAR, 2023) bottom-up emission inventory, with scaling applied in India, South Korea and China like for the a priori emission data (see Sect. 2.2). However, the resulting global emissions are further scaled to match TD estimates derived from the AGAGE 12-box model, as reported by Rigby et al. (2014) and Say et al. (2021). This scaling of the EDGAR emissions is motivated by the general large discrepancy to global TD estimates. Biases in the emissions provided to the reanalysis simulation would propagate into the baseline, thereby affecting global posterior emissions, leading to over- or underestimation depending on the baseline bias.

To further reduce possible errors and biases in the reanalysis, a simple data assimilation technique is applied which nudges modeled mole fractions towards measurements when particles reside within a specified spatio-temporal kernel around measurement locations. The nudging tendency or nudging increment Δm_{ij} for each particle (j) - measurement (i) pair is added to the simulated mass and is given by (Groot Zwaaftink et al., 2018):

$$\Delta m_{ij} = w_{s,ij} w_{t,ij} \frac{M_i - m_j}{\tau} \Delta t, \tag{1}$$

where $M_i - m_j$ represents the deviation between simulated particle mass (m_j) and measured mass (M_i). τ is the nudging relaxation timescale and Δt is the model synchronization time step. To ensure numerical stability, Δt is set to $900\,\mathrm{s}$ and τ to $1800\,\mathrm{s}$. $w_{s,ij}$ and $w_{t,ij}$ represent a spatial (s) and temporal (t) weight depending on the distance between each particle-measurement pair and are defined as:

$$w_{s,ij} = \left(1 - r_{ij}^2\right) I, I = \begin{cases} 1 & \text{if } r_{ij}^2 < 1 \\ 0 & \text{otherwise} \end{cases}, \tag{2}$$

where r_{ij}^2 follows:

$$r_{ij}^2 = \left(\frac{x_j - x_i}{h_x}\right)^2 + \left(\frac{y_j - y_i}{h_y}\right)^2 + \left(\frac{z_j - z_i}{h_z}\right)^2, \tag{3}$$

and

$$w_{t,ij} = \left(1 - \left|\frac{t_j - t_i}{h_t}\right|^3\right)^3. \tag{4}$$

x_j, y_j, z_j, and t_j refer to the particle's location and the current model time; x_i, y_i, z_i, and t_i refer to the measurement's location and sampling time. To adjust the impact of each individual observation station on the modeled mole fraction field, h_x, h_y, h_z, and h_t are introduced which define the spatio-temporal kernel extents in which particles are nudged. We choose kernel sizes based on the variability of measured mole fractions, ranging between $1° - 8°$ in horizontal, $100\,\mathrm{m} - 1000\,\mathrm{m}$ in vertical and $1\,\mathrm{d} - 10\,\mathrm{d}$ in temporal extent. Stations with smaller kernel extents are mainly situated in East Asia as they exhibit the highest mole fraction variability due to their close proximity to emission sources.

Daily mole fraction fields are output by FLEXPART11 LCM on a $3° \times 2°$ output grid on 10 vertical levels with upper boundaries at 0.1, 0.5, 1, 3, 5, 7, 10, 15, 25 and 40 km above the ground.

S3 Inversion method additions

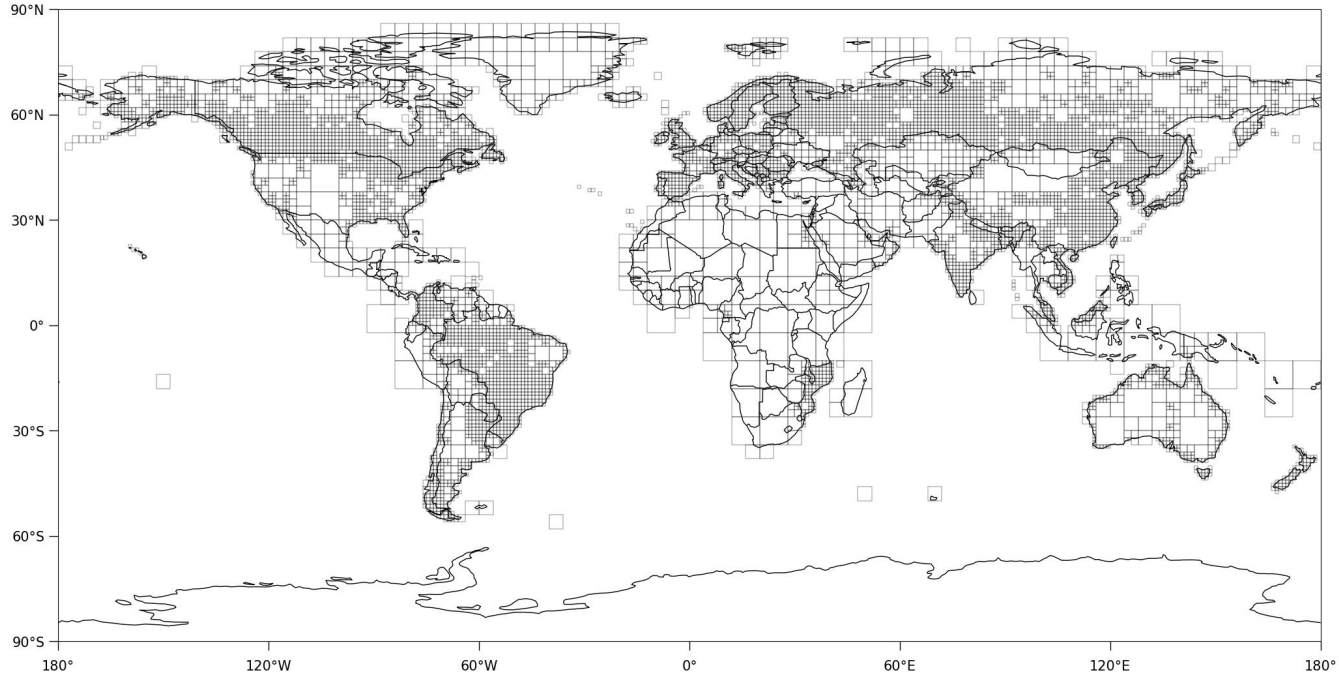

Figure S1. Variable inversion grid with excluded grid boxes over ocean and lowered resolution in less constrained regions and regions with low a priori emissions

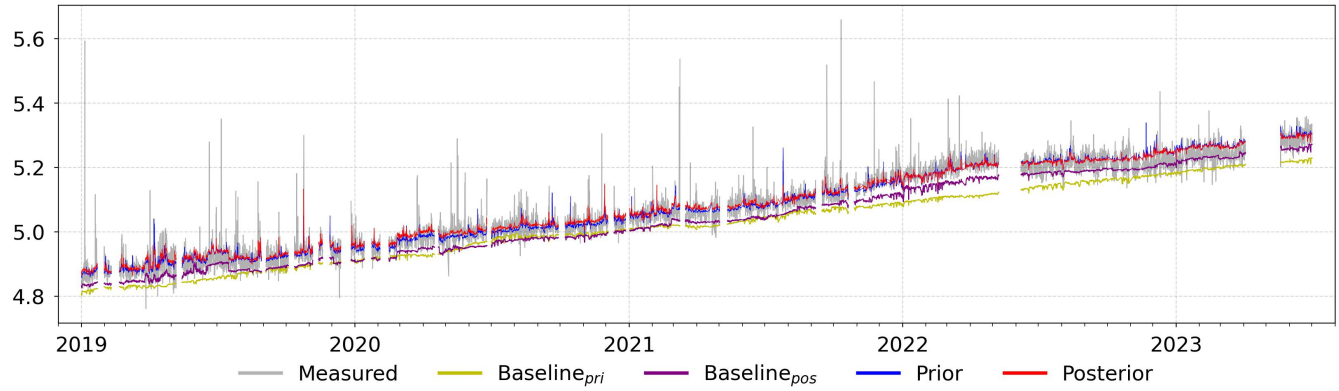

Figure S2. Measured (gray) and modeled a priori (blue) a posteriori (red), a priori baseline (green) and a posteriori baseline (violet) C_2F_6 mole fractions at Tacolneston (England)

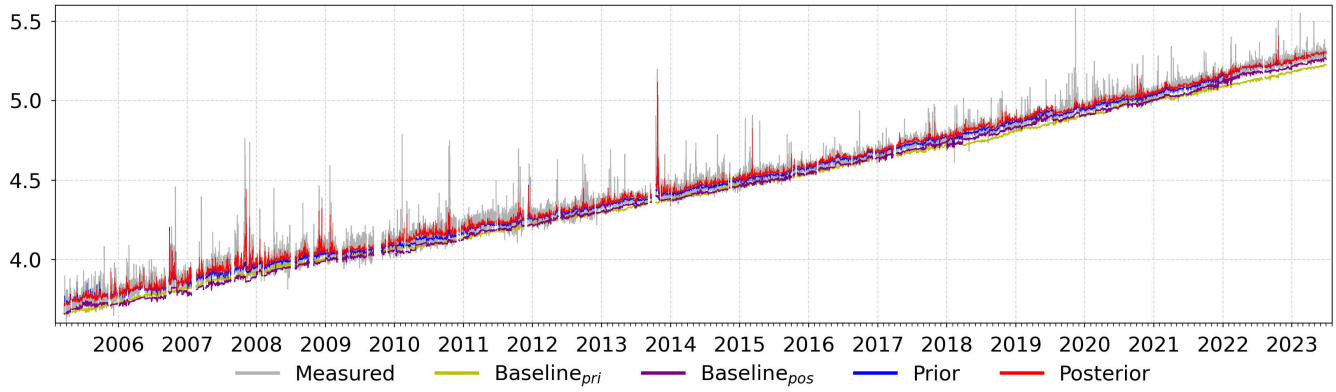

Figure S3. Measured (gray) and modeled a priori (blue) a posteriori (red), a priori baseline (green) and a posteriori baseline (violet) C_2F_6 mole fractions at Trinidad Head (USA, West)

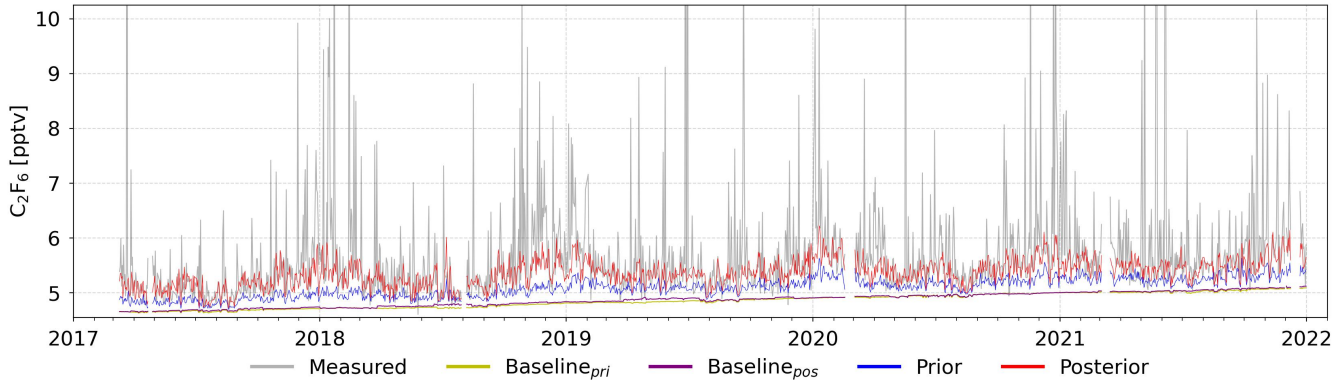

Figure S4. Measured (gray) and modeled a priori (blue) a posteriori (red), a priori baseline (green) and a posteriori baseline (violet) C_2F_6 mole fractions at Jiangjin, (China, South)

S4 Emission ratio distribution Asia

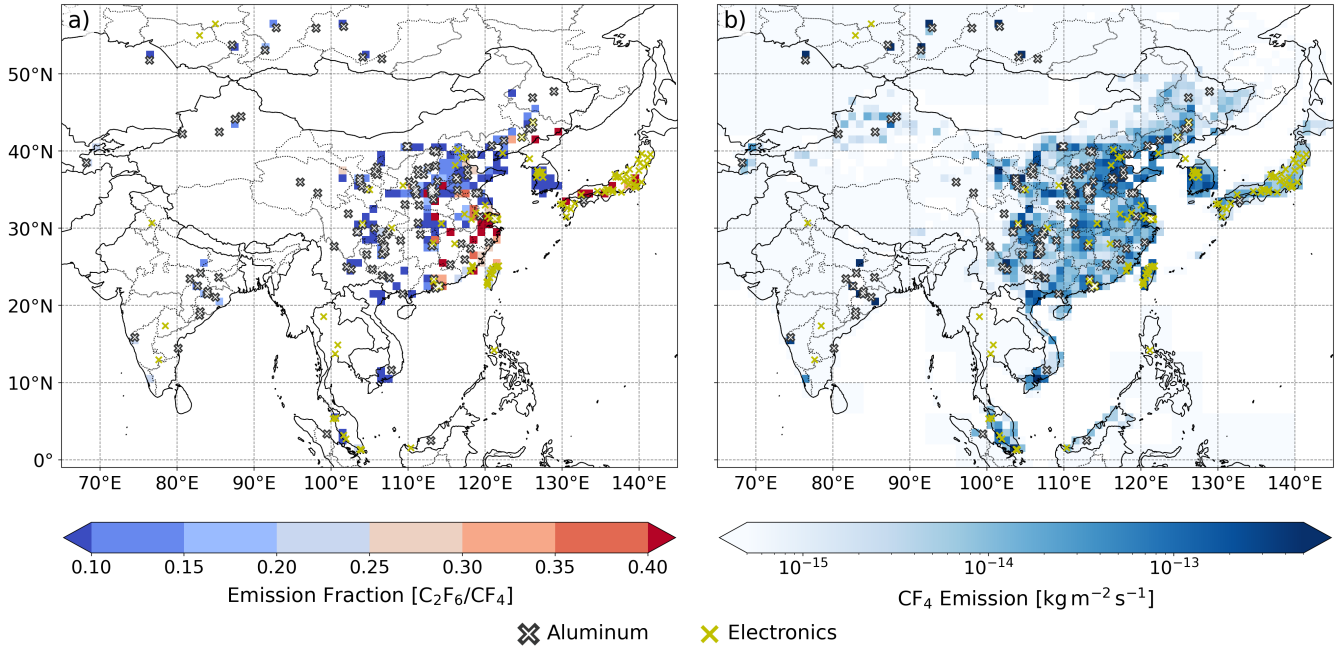

Figure S5. C_2F_6/CF_4 emission ratio (a) and CF_4 emissions (b) in large parts of Asia for the period 2018 – 2023. Also shown are the known locations of aluminum smelters (black crosses) and electronics factories (yellow crosses).

References

Bakels, L., Tatsii, D., Tipka, A., Thompson, R., Dütsch, M., Blaschek, M., Seibert, P., Baier, K., Bucci, S., Cassiani, M., Eckhardt, S., Groot Zwaaftink, C., Henne, S., Kaufmann, P., Lechner, V., Maurer, C., Mulder, M. D., Pisso, I., Plach, A., Subramanian, R., Vojta, M., and Stohl, A.: FLEXPART version 11: improved accuracy, efficiency, and flexibility, Geoscientific Model Development, 17, 7595–7627, https://doi.org/10.5194/gmd-17-7595-2024, 2024.

Chen, Y.: Available Data for "Inverse Modeling of High Global Warming Potential Perfluorinated Greenhouse Gases in Southeastern China", https://doi.org/10.7910/DVN/BFINPM, 2025.

EDGAR: Emission Database for Global Atmospheric Research, release version 8, European Commission, Joint Research Centre (JRC), the International Energy Agency (IEA), http://edgar.jrc.ec.europa.eu, 2023.

Groot Zwaaftink, C. D., Henne, S., Thompson, R. L., Dlugokencky, E. J., Machida, T., Paris, J.-D., Sasakawa, M., Segers, A., Sweeney, C., and Stohl, A.: Three-dimensional methane distribution simulated with FLEXPART 8-CTM-1.1 constrained with observation data, Geoscientific Model Development, 11, 4469–4487, https://doi.org/10.5194/gmd-11-4469-2018, 2018.

Rigby, M., Prinn, R. G., O'Doherty, S., Miller, B. R., Ivy, D., Mühle, J., Harth, C. M., Salameh, P. K., Arnold, T., Weiss, R. F., Krummel, P. B., Steele, L. P., Fraser, P. J., Young, D., and Simmonds, P. G.: Recent and future trends in synthetic greenhouse gas radiative forcing, Geophysical Research Letters, 41, 2623–2630, https://doi.org/10.1002/2013GL059099, 2014.

Say, D., Manning, A. J., Western, L. M., Young, D., Wisher, A., Rigby, M., Reimann, S., Vollmer, M. K., Maione, M., Arduini, J., Krummel, P. B., Mühle, J., Harth, C. M., Evans, B., Weiss, R. F., Prinn, R. G., and O'Doherty, S.: Global trends and European emissions of tetrafluoromethane (CF_4), hexafluoroethane (C_2F_6) and octafluoropropane (C_3F_8), Atmospheric Chemistry and Physics, 21, 2149–2164, https://doi.org/10.5194/acp-21-2149-2021, 2021.

Vojta, M., Plach, A., Thompson, R. L., and Stohl, A.: A comprehensive evaluation of the use of Lagrangian particle dispersion models for inverse modeling of greenhouse gas emissions, Geoscientific Model Development, 15, 8295–8323, https://doi.org/10.5194/gmd-15-8295-2022, 2022.